Autonomous Chemical-Sensing Aerial Robot for Urban/Suburban Environmental Monitoring

Xiang He, Joseph R. Bourne, Jake A. Steiner, Cole Mortensen, Kyle C. Hoffman, Christopher J. Dudley, Ben Rogers, Donald M. Cropek, and Kam K. Leang, *Member, IEEE*

***Abstract*—This paper describes the development of an autonomous chemical-sensing aerial robotic system for environmental monitoring in urban and suburban areas. The robot is equipped with a high-performance chemical sensor that identifies and quantifies chemical agents, enabling applications, such as chemical mapping, source localization, and estimation. To enable collision-free monitoring in areas with obstacles, such as in urban and suburban environments where buildings, trees, and other structures pose a challenge, a potential-field algorithm that incorporates past actions is used. A custom-designed ground station for controlling the robot, and planning and visualizing environmental data in real time is described. An empirical method is used to maximize the robot's flight time for improved effective operating range and to provide a safe operating standoff distance. Finally, two outdoor chemical dispersion experiments are conducted to demonstrate the capabilities of the autonomous airborne chemical-sensing system, where results show effective mapping of a propane gas leak.**

***Index Terms*—Chemical sensors, health and safety, mobile sensors, unmanned aerial vehicles (UAV).**

I. Introduction

FAST and effective environmental monitoring is needed immediately after accidents and natural disasters that involve leaks and spills of chemical, biological, radiological, nuclear, or explosive substances [1]–[4]. Mobile ground and aerial robots can be used to identify, isolate, track, map, and predict dispersions of such substances in an effort to minimize environmental impact and the threat to public health [5], especially for flammable gases and vapors which are often released in the gas-and-oil industry [6]. More specifically, autonomous aerial-robotic systems that combine an unmanned aerial vehicle (UAV) and advanced sensors with real-time data monitoring capabilities are well suited for assessment tasks because of their improved mobility over complex and challenging terrain. For instance, Fig. 1 shows the autonomous chemical-sensing aerial robot named Enif,[1] for sensing a simulated propane gas leak by scanning over terrain with dense undergrowth. In fact, mobile ground systems may find traversal over such terrain more challenging [7] compared to aerial systems. However, limited flight time and environments with obstacles are challenges that hinder the performance, functionality, and widespread adoption of the aerial vehicle technology, especially in urban and suburban settings [7]–[15].

Fig. 1. Chemical-sensing aerial robot named Enif[1] demonstrating the ability to autonomously scan for and map a propane gas leak. Portable wireless ground station for real-time data collection and monitoring not shown.

The design of an autonomous aerial chemical-sensing robotic system for environmental monitoring in urban and suburban areas is presented. The system, which has capabilities beyond the state-of-the-art, is built on a custom-designed high-performance multirotor aerial vehicle platform. The system is equipped with an advanced chemical sensor, automatic collision avoidance (CA) technology, autonomous flight capabilities, and a portable command station for mission planning and real-time data analysis. Although commercially-available platforms can be adapted for chemical sensing, where Fig. 2 summarizes the state-of-the-art, few platforms are designed to carry sensor payloads and additional computational hardware that enable operation beyond

Manuscript received April 3, 2018; revised August 7, 2018 and November 22, 2018; accepted February 12, 2019. Date of publication May 13, 2019; date of current version August 23, 2019. This work was supported in part by the University of Utah, in part by the National Science Foundation's Partnership for Innovation Program under Grant 1430328, and in part by the U.S. ARMY STTR Program W9132T-16-C-0001. *(Corresponding author: Kam K. Leang.)*

X. He, J. R. Bourne, J. A. Steiner, C. Mortensen, K. C. Hoffman, and K. K. Leang are with the Design, Automation, Robotics, and Control (DARC) Lab, University of Utah Robotics Center and Department of Mechanical Engineering, Salt Lake City, UT 84112 USA (e-mail: xiang.he@utah.edu; joseph.bourne@utah.edu; Jake.Steiner@utah.edu; cole.mortensen@utah.edu; Kyle.C.Hoffman@utah.edu; kam.k.leang@utah.edu).

C. J. Dudley and B. Rogers are with the Nevada Nanotech Systems, Inc., Sparks, NV 89431 USA (e-mail: cj.dudley@nevadanano.com; rogers@nevadanano.com).

D. M. Cropek is with the U.S. ARMY CORPS, ERDC-CERL, Champaign, IL, USA (e-mail: Donald.M.Cropek@usace.army.mil).

Digital Object Identifier 10.1109/JSYST.2019.2905807

[1]Named after the star at the end of the nose of the constellation Pegasus.

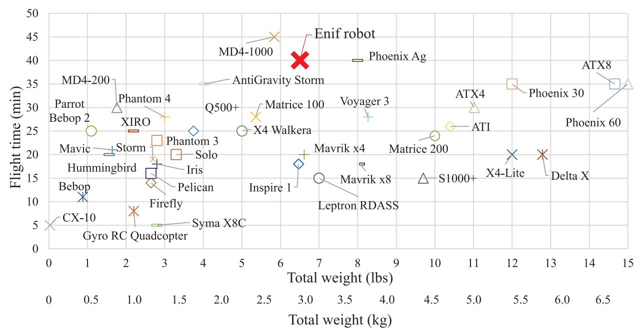

Fig. 2. Survey of commercially available aerial robot platform showing hovering flight time and gross vehicle weight (GVW) compared to the Enif design.

20 minutes. Thus, the system described herein differentiates itself from prior systems [7]–[15] by incorporating flight-time enhancement design methodologies, the integration of CA technology, and the use of a new chemical sensor capable of identifying chemical substances, reporting concentration values, and providing atmospheric information (such as humidity, temperature, etc.). Thus, not only is the integrated system lightweight and portable, it can

1) cover larger areas compared to existing systems (for a given flight pattern) permitting operation from a safe standoff distance (approximately 8 km or 5 miles);
2) be deployed in urban/suburban environments (e.g., where obstacles are present, such as buildings and/or trees);
3) collect chemical and atmospheric data in real time;
4) quickly display concentration mapping data to a custom ground station for reconnaissance applications.

Systematic evaluation of critical parameters and the understanding of performance limitations are needed to develop a functional and high-performing system. An empirical modeling approach is described that enables the flight time of the vehicle for a given configuration to be achieved. The approach predicts vehicle thrust generation as a function of available power (i.e., battery capacity and weight), motor characteristics, and propeller performance. Furthermore, the model considers a large database of battery options and motor and propeller designs. Similar to previous works [16]–[20], the objective is to systematically choose the appropriate combination of motors, propellers, and battery, while minimizing frame weight, avionics power, etc., to achieve a desired flight time. This empirical approach is tailored to the specific hardware in use and incorporates complex phenomenon, such as aerodynamic nonlinearities and elevation differences. It is pointed out that momentum theory-based optimization of flight time used in the past does not consider elevation differences, thus usually overestimates the flight time [16], [17], [19], [21], [22].

Urban and suburban environments affected by dangerous spills and leaks often have obstacles, such as trees, buildings, or other structures that pose a challenge. Effective monitoring of such environments requires the mobile sensor system to automatically avoid collisions. Herein, a modified potential-field (PF) algorithm that incorporates past actions (PF-IPA) is presented and implemented for collision-free control of the robot between waypoints. This approach is simple, efficient, and outperforms traditional PF algorithms, which can often get trapped in local minimums [23]. The algorithm utilizes the information from a two-dimensional (2-D) scanning rangefinder to control the robot's inputs to jointly avoid obstacles and move toward a desired waypoint.

There are four main contributions of this work. First, an empirical method is described to maximize the flight time of the aerial robotic system beyond the current state-of-the-art electrically-powered systems that weigh less than 8 lbs (3.6 kg). Second, a new chemical sensor capable of both identification and quantification is developed, characterized (for two example analytes), and tested for chemical mapping. This sensor has response times on the order of several seconds and lower power consumption compared to widely used metal oxide (MOX) chemical sensors with response times greater than 30 s. Third, a new reactive CA algorithm based on the PF framework that incorporates past actions is developed and tested. Simulation and experimental results show that the CA algorithm can handle urban and suburban areas with confinements (PF local minima). Finally, outdoor field tests are conducted to demonstrate effective autonomous mapping of a propane gas leak. To the best of the authors' knowledge and compared to similar research platforms, the proposed system illustrates a more complete and comprehensive autonomous chemical-sensing aerial robot system.

The paper is organized as follows. Section II reviews the state-of-the-art research on outdoor chemical-sensing systems. Section III describes the design process for maximizing vehicle flight time. The details of the chemical sensor is described in Section IV. The ground station, software structure, and communication system are discussed in Section V. Section VI describes the robot control algorithms, including CA used for motion planning. Section VII presents the outdoor field test and experimental results. Finally, concluding remarks are given in Section VIII.

II. Related Works

Environmental monitoring can be accomplished by two distinct approaches: Using a static sensor network (SSN) and/or a mobile sensor network (MSN) [3]. In an SSN, fixed sensors are distributed over an area of interest (AOI) for monitoring. These sensor networks can provide early detection for critical infrastructure, but they require initial setup time and a dense grid of sensors for high resolution monitoring. Furthermore, the spill/leak must be within the area where the SSN is placed. An example application of SSN is source term estimation of a hazardous source using 60 sensors as described in [24].

In a MSN, mobile platforms (ground, air, or water-based) carry sensors for monitoring and information gathering [25]. For example, in [26], the ground robot Gasbot was used to map chemical vapors, such as hydrogen and sulfide in decommissioned landfills. Although this work was expanded upon in [8], where a quadcopter aerial robot was used to overcome challenges in traversing a landfill environment, the aerial robot had limited autonomy. One advantage of MSN is that a small number of mobile sensors can achieve similar performance as larger SSN for chemical tracking [27].

To improve the environmental monitoring capabilities, such as concentration mapping of airborne contaminants, aerial robots have obvious advantages over ground robots. For example, aerial platforms are more versatile, maneuverable, and can potentially accomplish the same task more efficiently, especially over complex terrain. However, aerial robots must be able to fly for extended periods of time to survey large areas far from the command station and/or deployment point. Interestingly, the majority of prior work ignores the crucial factor of flight time [8], [10], [11], [28]–[33]. Furthermore, to survey and monitor realistic urban and suburban environments, aerial chemical-sensing systems must be able to avoid obstacles. However, prior research [8], [10], [11], [15], [28]–[34] primarily assumes no obstacles exist, therefore the works do not consider CA. Unfortunately, physical contact with obstacles can cause damage to the monitoring system and environment, and even introduce contamination and can affect the measurements.

There are two main classes of aerial robot platforms for environmental monitoring: fixed-wing and multirotor systems [25]. For example, a fixed-wing aerial robot with solar panels located along the wings is described in [35]. Likewise, an integrated ocean observing system using a fixed-wing aerial robot is presented in [36]. Fixed-wing-based systems often fly high to avoid obstacles and have longer flight times compared to multi-rotor robots. However, the ability to hover is advantageous for thoroughly investigating a specific location, as well as supporting chemical sensors with low-frequency performance. Therefore, rotor-based chemical-sensing aerial robots capable of hovering have attracted significant attention [8], [10], [11], [15], [28]–[34].

There are many ways to extend the flight time of rotor-based aerial robots capable of hovering. For example, in [37], they explored a hybrid-based powered aircraft for carrying heavy payloads [38]–[40]. In [41]–[43], they investigated a vertical takeoff aircraft design to improve the range of the aerial system, and in [44]–[47], they incorporated additional motors/propellers (such as hexacopter or octocopter) for redundancy, achieved high flight times, and payload capabilities. However, these designs are beyond the scope of this research because of the heavy gross vehicle weight (GVW) (above 10 kg) due to the additional power sources and motors, large footprints (more propellers require more space), and increased cost. Furthermore, some of these designs are impractical for chemical sensing. For example, it is possible that the exhaust could interfere with onboard chemical sensing, and finally, because of the low-frequency nature of chemical sensors (typically 10–20 s), designs which require constant movement may operate outside of a sensor's bandwidth. For these reasons, this paper focuses on developing an electrically powered multirotor vehicles with the ability to hover for chemical sensing.

The empirical approach taken to extend flight time is a general process and can be applied to all of the previously discussed designs. Although several works have considered the flight-time challenge from a more theoretical point of view [15], [21], [34], [48], the outcomes are often an over estimate of the expected flight time due to unmodeled influences. Besides, hardware dedicated to sensing and computing is usually regarded as payload (without considering power consumption) and is not considered in the flight-time calculation as in previous works [19], [48], [49]. Herein, an empirical approach, which takes into account actual hardware (i.e., motors, propellers, and batteries), is used. Therefore, unmodeled influences, such as changes in elevations or hardware differences can be accounted for in the modeling process. Furthermore, the empirical flight-time prediction considers not only the weight of the platform, but also the particular choice of the motor, propeller, and battery configuration, which has been determined to be coupled to the flight-time performance.

State-of-the-art designs of chemical-sensing aerial platforms offer limited performance when navigating realistic and unknown environments with possibly complex obstacles, such as trees. Herein, a computationally efficient reactive CA algorithm using a 2-D scanning rangefinder sensor is described and implemented. There are two ways to approach the CA and motion planning problem: Using map-based and/or reactive techniques. Map-based methods [50]–[57] use or create a map and utilize a global planner to help circumvent obstacles in the environment. Global methods rely on maps of the environment being known *a priori* or to build a map while traveling. Maps can be computationally expensive to build and can suffer from inaccuracies in localization, which is common with GPS. Reactive CA methods use a perception-action process [58], which allows the algorithm to deal with unknown or changing environment, as well as inaccuracies in localization. PF-based methods [59] are widely used as reactive planners due to their simplicity and computational efficiency. They do, however, have some inherent drawbacks as described in [23] including getting trapped in local minima and oscillation in narrow passages. There have been several approaches to reduce the effect of these drawbacks including adding a random force [60] and avoiding the past [61]. Both of these methods have limited abilities to work in the wide variety of obstacles encountered outdoors, but could be tuned to work in a specific environment. A method of altering the PF, which allows for successful CA among many types of obstacles, is described. This method has been shown to perform reliably with sensor noise and GPS error inherent in outdoor environments.

III. Aerial Chemical-Sensing System

A. *Key Components of the Aerial Robotic Sensing System*

A summary of the key components of the aerial vehicle is shown in Fig. 3(a), where a flight controller (DJI A3) is paired with a single-board-computer (Odroid C2) for computation and autonomous control. The majority of the structural components were designed and manufactured in house, while other components, such as the electronic speed controllers, flight controller, flight computer, battery, etc., are off-the-shelf components. A summary of the weight of each component is shown in Fig. 3(b). An empirical approach is utilized, which carefully selects a battery weight that maximizes the flight time [see Fig. 3(b)], where in this case, the battery weight is approximately half of the GVW of the system [34].

B. *Flight-Time Analysis*

The empirical approach to maximize the flight time depends on models of battery capacity and current drawn from the motor/propeller system. Once these empirical models are obtained, one can choose the most adequate motor, propeller, and battery combination, while the payload is held fixed according to

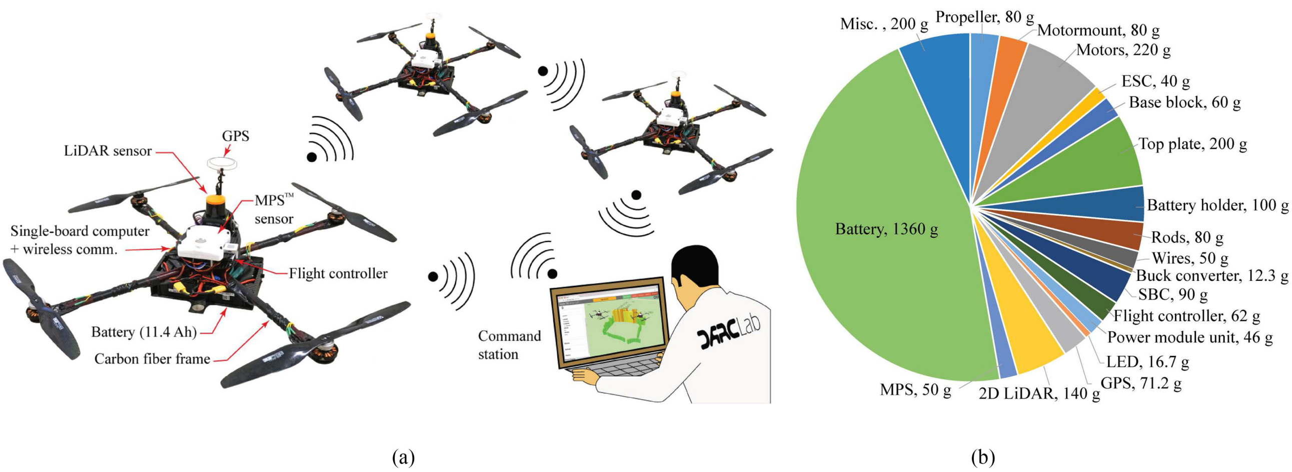

Fig. 3. Overview of the Enif autonomous aerial robot chemical-sensing system. (a) System consists of multiple vehicles that can operate through a wireless network and communicate with a ground station with data analysis capabilities. (b) Weight of the individual components, where the battery weight is approximately 50% of the gross vehicle weight.

Fig. 4(b). Herein, configurations are limited to a discrete set, including four brushless motors from 300 to 400 KV, five propellers sets from 13 to 16 in, and over 500 different types of batteries. It is pointed out that T-Motor's MT4004 brushless motor [62] is found to be the most efficient with respect to the vendor's data [63], as well as experimental validation (results not included for brevity), thus the following presents flight-time analysis with respect to this motor.

Flight time t_f is calculated through dividing the battery capacity by the total power consumption [16]–[18], [20]

$$t_f = \frac{C_b}{4V_b i + P_a} \tag{1}$$

where C_b is the capacity of the battery as a function of weight of the battery [see Fig. 4(a)], V_b is the average voltage of the battery, i is the current as a function of hovering thrust T_{hov}, diameter d, and pitch p of the propeller, and finally, P_a is the power consumption due to the avionics. The thrust required at hover (neglecting atmospheric disturbances) as a function of the GVW is given by

$$T_{\text{hov}} = W_b + W_f + W_s + W_m \tag{2}$$

where W_b is the weight of the battery as a function of its capacity, W_f is the weight of the frame, W_s is the payload (i.e., sensors) weight, and W_m is miscellaneous weight, such as weight of wires and additional hardware. Here, the current i and battery capacity C_b are obtained via linear and exponential fitting techniques, respectively, which are shown in Fig. 4(a) and (b). More specifically, battery data is obtained from the vendor, for example [63], and current versus thrust data is obtained from the vendor and experimentally. Fig. 4(c) shows flight-time curves for varying GVW, i.e., W_f, W_s, and W_m were fixed according to Fig. 3(b), while changing W_b, thus the capacity according to Fig. 4(a). It is emphasized that Fig. 4(c) was obtained using the linear battery model given in Fig. 4(a), i.e., this is an average model of batteries. From this curve, it can be seen that the 38-cm diameter by 13-cm pitch (15 × 5.0 in) propeller is the most efficient with the selected motor.

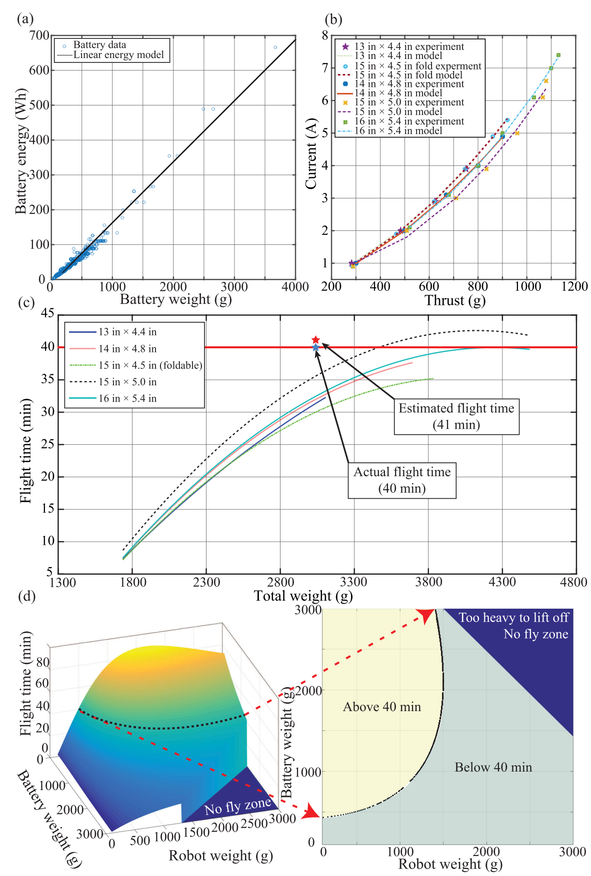

Fig. 4. (a) Linear battery model of capacity as a function of battery weight. Blue dots mark the data from the vendor and the solid line is the linearly-fitted-battery-energy model. (b) Exponential motor-propeller model of motor (T-motor MT4004) current as a function of thrust for five sets of propellers, with diameter ranging from 0.33 m (13 in) to 0.41 m (16 in). Dots mark the experimental data. (c) Flight-time prediction (of the motor T-motor MT4004) for various total weight by varying the battery weight, while fixing the robot weight. These curves were generated using the models in (a) and (b). (d) Left: Flight-time surface with the selected motor (T-Motor MT4004) and propeller (15-in diameter × 5.0-in pitch) pair for various robot configurations, i.e., for various robot weights and battery weights. (d) Right: Illustrates all robot configurations (robot weight and battery weight) that will achieve 40-min flight time.

Fig. 4(d) shows the surface plot of the flight time for the selected motor and propeller across various battery weights W_b and aerial robot weight without battery $(W_f + W_s + W_m)$. From this surface, one can choose a battery weight, and subsequently, the battery capacity due to the linearity of this relationship [see Fig. 4(a)] and the robot weight without the battery for a desired flight time. For example, Fig. 4(d) shows all aerial robot configurations that will achieve $t_f \approx 40$ min, with respect to the various models in Fig. 4(a) and (b).

From this analysis, a battery with 11.4 Ah was chosen by combining two 5.7-Ah batteries in parallel. This configuration resulted in a lightweight, compact, and portable battery system. As shown in Fig. 2, achieving 40-min flight time is not trivial and requires careful selection of hardware components and GVW. Note that the 5.7 Ah batteries were chosen due to its high energy density specifications with respect to the energy model in Fig. 4(a), i.e., this battery's performance exceeds the model's prediction. With a GVW equal to 2.95 kg (6.51 lbs) and the 11.4-Ah battery, it was predicted that the flight time would be approximately 41 min as shown in Fig. 4(c). After testing, it was determined that the platform was able to achieve 39 min 46 s of flight time, indicating good agreement between the empirical model and experimental results. The prediction and actual flight times are above the propeller 38 × 13 cm (15 × 5 in) curve in Fig. 4(c) because this curve used an average model of the batteries. It is pointed out in Fig. 4(d) that there is a region where the battery weight is such that the vehicle is too heavy to fly, thus increasing battery weight may not necessarily lead to increased flight time since the battery capacity is limited.

IV. Molecular Property Spectrometer (MPS) Chemical Sensor

One of the highlights of the Enif system is its chemical sensor, the NevadaNano's MEMS-based MPS Flammable Gas Sensor.[2] The sensor has built-in environmental compensation and the ability of detecting and accurately quantifying a wide range of flammable gases [64]. The MPS is intrinsically safe, robust, compact, lightweight, and extremely poison resistant. It is developed to detect and classify a variety of flammable gases, including methane, propane, butane, ethane, ethylene, hexane, hydrogen, isopropanol, pentane, propane, propylene, toluene, and xylene, among others at concentrations from 1% to 100% of their respective lower explosive limit (LEL) values. Utilizing the measured thermal properties of the current ambient air/gas mixture to which it is exposed, the MPS automatically applies the appropriate conversion factor in real time to provide accurate %LEL concentration reporting for the various analytes noted [64]. Additionally, the MPS reports atmospheric conditions, including temperature, humidity, and pressure. In order to plan appropriate wait times at each waypoint during measurements, modeling of the sensor, including the response dynamics, is critical. Characterization of the MPS and commonly used MOX with experimental results showing the sensors' response times associated with methane and propane gas are presented as follows.

[2]http://www.nevadanano.com

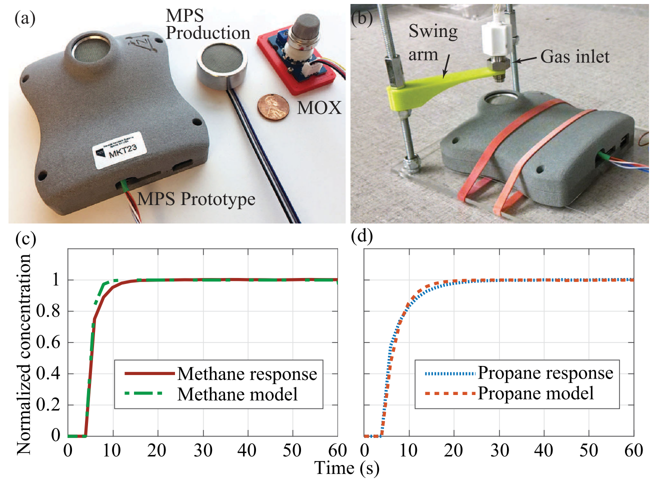

Fig. 5. (a) MPS prototype sensor compared to the MPS production sensor and a MOX sensor. (b) Swingable arm fixture for characterizing chemical sensor. (c) and (d) Experimental and modeled responses for the MPS sensor upon exposure to 50% LEL propane and 50% LEL methane. Concentration of 50% LEL is normalized.

TABLE I
Comparison of Key Sensor Characteristics—MPS and MOX

	MPS (Prototype)	MPS (Production)	MOX
Response time (s)	10-17	3-5	10-15
Usable life-span (years)	>5		3-5
Form factor (cm^3)	≈360	≈14	≈45
Power consumption (mW)	275	56 (avg)	200-800
Relative cost ($)	N/A	200	<30
Preheat time required (min)	0		30-60
Calibration interval (months)	>12		≈3
Selectivity	Multiple gas ID		None

A. Comparison of Characteristics - MPS and MOX Sensors

Although a number of sensor options exist with respect to general gas detection, for gas sensing leveraging mobile robots, MOX sensors are often utilized for *in situ* sensing [65]. Fig. 5(a) shows the MPS prototype sensor compared to the MPS production sensor and an MOX sensor. As noted in Table I, comparing key characteristics between the MPS and MOX sensors, the MPS shares many of the advantages of widely used MOX sensors, including relatively fast response time, relatively long usable lifespan, and a small form factor. Both sensors also exhibit relatively low susceptibility to changes in environmental conditions [66], [67]. However, one key advantage of the MPS is that no preheating time is required prior to operation, critical in situations when immediate environmental monitoring is needed. The MPS also offers an extended calibration interval in comparison with MOX and other similar sensors. Also, the primary advantage of the MPS is its ability to classify specific analyte's molecular properties, using within-unit processing of multiple sensor inputs, including environmental parameters, with real-time chemometric algorithms [64]. Additionally, poison robustness is a considerable benefit of MPS as it measures the thermal properties of the air and does not rely upon a chemical reaction at the sensor surface. The MPS also offers improved response

TABLE II
MPS SENSOR RESPONSE TIMES

	Methane	Propane
Prototype response time (s)	10.0	17.0
Production response time (s)	2.8	3.8

times as compared to majority of MOX sensors [68] and does not exhibit the common issues of hysteresis and sensor drift.

B. Sensor Characterization

Through experimental testing, the response time of the prototype version of the MPS were characterized for two target analytes methane and propane at concentration levels equivalent to 50% LEL for each of these gases (25 000 and 10 500 ppm, respectively). In performing the tests, a swingable arm fixture was used to hold the outlet of a supply line providing calibration-grade 50% LEL propane or methane at a regulated volumetric flow rate of 500 ml/min. This fixture enabled the regulated flow of gas to be quickly applied to and removed from the sensor, providing a "step-like" input supporting response time assessment [see apparatus in Fig. 5(b)]. Average response times of the prototype MPS using this method for the two target analytes are provided in Table II and the corresponding experimental and model-predicted responses are shown in Fig. 5(c) and (d). A linear first-order dynamic system model with a delay function was used to model the sensor behavior. Rise times represent the elapsed time from gas source application to the sensor to the attainment of the concentration value equivalent to 95% of the average steady state value for each respective case. The responses of the MPS are well represented by the first-order model described in the following transfer function:

$$\frac{Y(s)}{R(s)} = \frac{e^{-as}}{\tau s + 1}, \quad \tau, a = \begin{cases} \tau_{\text{rise}}, a_{\text{rise}} & r'(t) > 0 \\ \tau_{\text{rec}}, a_{\text{rec}} & r'(t) \leq 0 \end{cases} \tag{3}$$

where $Y(s)$ represents the Laplace Transform of the expected sensor output for a given reference input $R(s)$, τ_{rise} and τ_{rec} are the system time constant for rising and falling, respectively, and a is the delay time.

In a recent development, NevadaNano has now created a product version of the MPS [see Fig. 5(a)] with improved features, including a smaller form factor, reduced power consumption, and improved response times. Additional details regarding the production version of the MPS are provided in Table I and associated response times obtained through initial laboratory testing at NevadaNano are provided in Table II.

V. GROUND STATION, COMMUNICATION, AND MISSION CONTROL

A user-friendly ground station is developed to control the aerial robot and review sensor information during a mission. The ground station allows users to select an AOI on a map and monitor live sensor information as it is collected by the robot. All communication between the ground station and the robot is done using the Robot Operating System (ROS) software framework (see Fig. 6) [69], which also handles the multistream data syncing and interunit communication between robots.

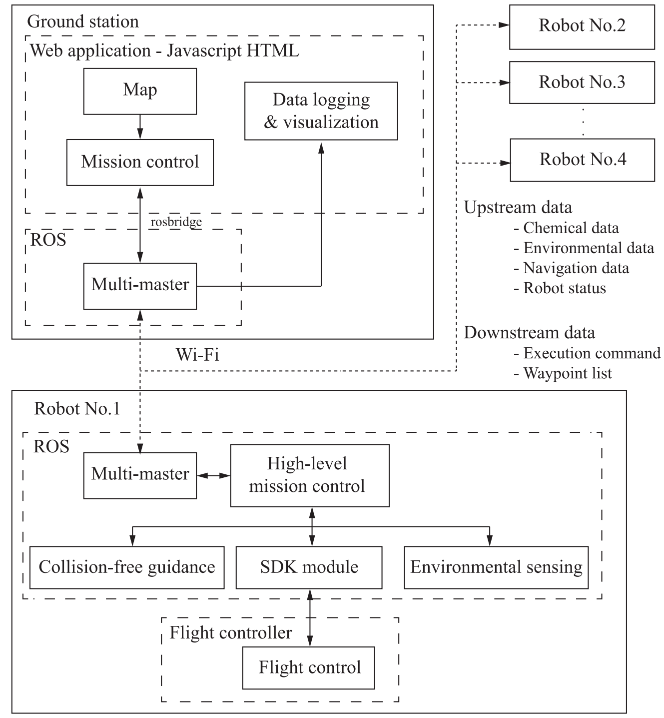

Fig. 6. Communication and software configuration diagram. Solid arrows represent data flow between nodes. The system is designed to have the ability of controlling multiple robots with single ground station. Multistream data syncing and communication is handled by the ROS framework and the onboard multi-master node.

A. Ground Station Hardware and Software

The Enif ground station hardware consists of a laptop and an outdoor wireless access point. The access point broadcasts a secure Wi-Fi network (shown as dashed line in Fig. 6) that both the aerial robot and the laptop are connected to. It has been experimentally determined that the range of this access point is limited to 200 m in an urban environment with buildings and trees. Additional range can be achieved using other wireless communication options, including radio-frequency (RF) communication, for ranges beyond 1 km.

The ground station software is developed as a web application using JavaScript, HTML, and CSS. To overcome the challenge that network access might be unavailable, all components of the ground station software (see Fig. 6) are self-hosted on the ground station laptop, which includes a web server for the web application as well as a map server for the map interface. The ROSbridge ROS package is used to provide a link between the JavaScript of the web application and ROS running on the aerial robot. There are following five main software components on the robot:

1) multimaster (managing communication);
2) high-level mission control;
3) collision-free guidance (see Section VI);
4) software development kit module (interfacing with flight controller);
5) environmental sensing (sensor driver).

The high-level mission control interprets and executes commands from the ground station, such as takeoff and landing, as well as handling the waypoint logic and sensor data packing.

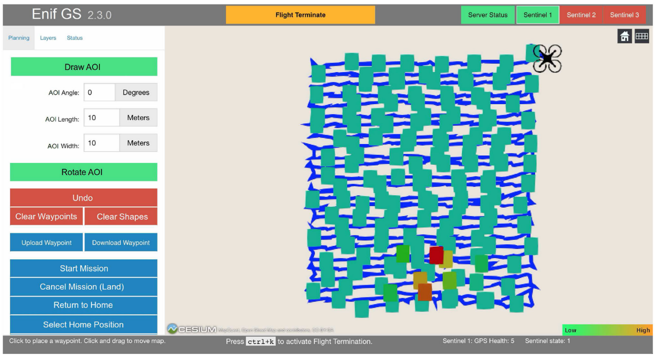

Fig. 7. Example GUI of the ground station software with heat map of raster scan results indicating sensed propane source.

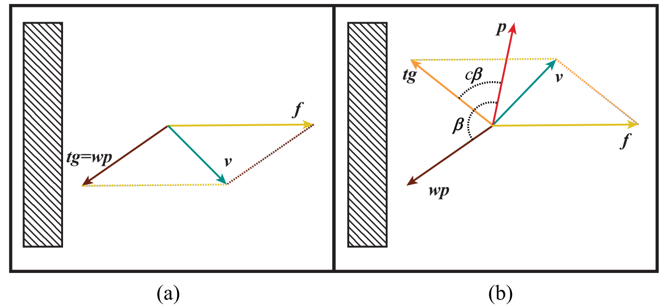

Fig. 8. Demonstration of vectors used in (a) PF and (b) PF-IPA. The drastic difference in the action vector $\mathbf{v}$ results from the dynamics of the attractive force $\mathbf{tg}$ in PF-IPA.

Mission parameters, such as waypoint wait time, flight altitude, and velocity, can be configured from the *Planning* tab, as well as the mission operation, i.e., start mission, land, and return to home. The left-hand panel of Fig. 7 shows these options in the user interface. Sensor data is packed with the robot's number and the most recent GPS coordinate of the robot. The package is then broadcasted to the ground station and other robots in real time through ROS, via the Wi-Fi network.

Sensor data is relayed to the ground station in real time via the Wi-Fi network. Users can select between six data types provided by the chemical sensor: %LEL, temperature, pressure, humidity, absolute humidity, and humid air density. The selected sensor information is displayed to the user in the form of a color-coded customized heat map. The customized heat map records the highest reading within the size of the aerial robot (0.6 m) with respect to the last recorded position and displays a colored square proportional to the reading. Display of the heat map, trajectory, and waypoint lies under the *Layer* tab. A concentration map of a raster scan over a propane source can be seen in Fig. 7.

B. *Mission Control*

Waypoints can be generated in two ways. A user can click locations on the map that they would like the aerial robot to inspect. The user can also specify an AOI by clicking *Draw AOI*, clicking the center of the AOI on the map, typing in the width, height, scanning angle, and step length between waypoints. If a particular area is going to be scanned multiple times, waypoint files can be downloaded for later use. This eliminates the need of replacing waypoints when starting a new mission from scratch.

A typical work flow for an environmental monitoring mission is as follows.

1) Select AOI or waypoint(s). Robot will not takeoff until at least one waypoint is specified.
2) Adjust flight parameters, such as altitude and velocity (default as 2 m and 1 m/s, respectively).
3) Setup the robot on a flat surface and click *Select Home Position.*
4) Launch the robot by clicking *Start Mission* and it will automatically start scanning the area.
5) (Optional) Dynamically adding waypoint to the existing list does not affect the current behavior of the robot. It only changes the size of the list.
6) (Optional) Click *Layer* tab to select which environmental data to display.
7) Mission will be executed in a loop by default. Click *Return to Home* to bring the robot to the specified home position.
8) *Cancel Mission (Land)* will make the robot land immediately and the mission will restart from the first waypoint in the event that *Start Mission* is again executed.

VI. Collision Avoidance Algorithm

The proposed CA algorithm is a reactive method that makes decisions based on the distance information from a 2-D scanning rangefinder with a 270° field of view. Prefiltering with a moving average filter is implemented to reduce noise. The scan is then segmented into arcs of angle α. For each segment, the shortest distance is used as the radius of the arc. Segmenting the scan reduces the amount of calculations in the CA algorithm.

A. *Potential Field that Incorporates Past Actions (PF-IPA)*

To overcome some of the well-known shortcomings of PF [23], a new PF-IPA is described. It is a modification of the standard PF algorithm. In standard PF, the action vector sent to the robot is the addition of an attractive vector toward the goal and a repulsive vector away from obstacles. The target vector $\mathbf{tg}$ is used as the attractive force and is found with $\mathbf{tg} = \mathbf{wp}$ [see Fig. 8(a)], where $\mathbf{wp}$ is a vector in the direction of the next waypoint from the current location. The repulsive vector away from obstacles is created with the following relation:

$$\mathbf{f}' = \sum_{i=1}^{p} \frac{-a\mathbf{r}_i}{||\mathbf{r}_i||^b} \tag{4}$$

where $\mathbf{r}_i$ is the range vector of each reading in the scan, and p is the number of readings in the scan. Constants a and b are parameters that can be adjusted to change the behavior of $\mathbf{f}'$. To insure stable flight around obstacles, the magnitude of the repulsive force is saturated to some max value M

$$\mathbf{f} = \begin{cases} \frac{\mathbf{f}'}{||\mathbf{f}'||}M, & \text{if } ||\mathbf{f}'|| > M \\ \mathbf{f}', & \text{otherwise.} \end{cases} \tag{5}$$

The action vector $\mathbf{v}$ sent to the flight controller is found with

$$\mathbf{v} = \mathbf{f} + \mathbf{tg}. \tag{6}$$

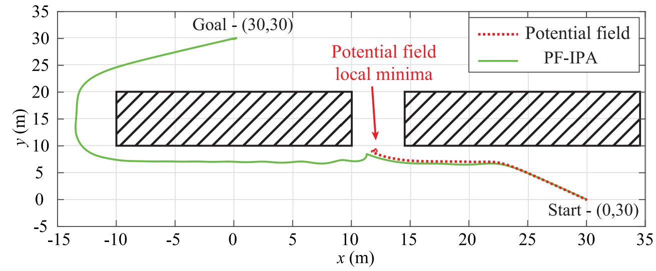

Fig. 9. Simulation of guiding aerial robot from start to goal using PF (dash red) versus PF-IPA (solid green). The red dashed curve ends between the two obstacles where the attractive and repulsive force cancel out.

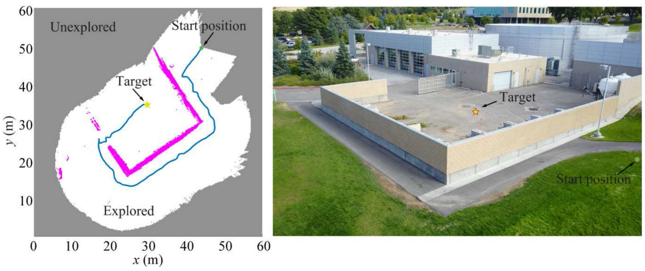

Fig. 10. CA experimental results. (a) Outdoor flight test demonstrating navigation around an urban obstruction from Waypoint 1 to Waypoint 2 with the PF-IPA. The aerial robot was tethered during the test. (b) Postprocessed map showing the two waypoints, robot trajectory (blue solid curve), and the obstruction (purple dots, acquired by the robot).

The magnitude of $\mathbf{v}$ is saturated to the velocity parameter set by the user. In the absence of obstacles, $||\mathbf{f}||$ is zero, leading $||\mathbf{tg}||$ to be the action vector in open space. The relative magnitude of $\mathbf{f}$ and $\mathbf{tg}$ determines how much influence the target has on the overall commanded direction in the presence of obstacles.

Standard PF has a few well-known drawbacks, such as getting stuck in local minima and oscillating between two obstacles. To enable the robot to navigate out of many local minimas and to traverse the environment more smoothly, a new method of modifying the attractive force with the past actions is implemented. The improvement to the standard PF is shown in Fig. 9, a scenario where the standard PF gets trapped in a local minima, where $\mathbf{tg}$ and $\mathbf{f}$ cancel out leaving $\mathbf{v} = 0$. By adding a modification on the attractive force, it is then shown that the motion planning is improved and the robot successfully navigates to the goal location using PF-IPA.

To incorporate past actions into the attractive force, a vector of the past actions $\mathbf{p}$ is first created from the past n action vectors

$$\mathbf{p} = \sum_{i=k-n}^{k} \mathbf{v}_i \tag{7}$$

where k is the time step of the current command. Each time the goal changes, i.e., the waypoint is reached, k is reset to zero. The angle of $\mathbf{p}$ will be used to modify the angle of the target vector $\mathbf{tg}$ in (6). Incorporating past actions adds inertia to the robot's decisions based off the previous commands. It will cause the robot to commit more to a decision. The longer the robot travels in a direction, the more it will resist change from that direction. Instead of adding a force vector directly to the action vector $\mathbf{v}$ [61], the angle of the target vector $\mathbf{tg}$ is modified based on β, the angle from $\mathbf{p}$ to $\mathbf{wp}$. The target vector angle is found with

$$\theta_{\mathbf{tg}} = \begin{cases} \theta_{\mathbf{wp}}, & \text{if } k < n \\ \theta_{\mathbf{p}} + c\beta, & \text{otherwise} \end{cases} \tag{8}$$

where the parameter $c \in (0, 1]$ needs to be experimentally tuned based on the desired behavior. The vectors used in the PF-IPA method are shown in Fig. 8(b). In a simulated environment the improvement of PF-IPA compared to PF is shown in Fig. 9. The robot using PF-IPA successfully avoids the local minima that trapped PF and reaches the goal.

B. Waypoint Logic

The motion planner attempts to consecutively travel between all waypoints sent from the Enif ground station. A proportional controller on yaw is implemented to keep the blind spot of the rangefinder in the opposite direction of the velocity vector. The height, which is set by the user, is controlled with a proportional–integral–derivative (PID) controller and is sensed with a downward facing LiDAR rangefinder. The maximum ascent and descent velocities are saturated at 2 m/s to maintain stability. Once the robot is within a certain radius of the waypoint, it is considered reached. The robot will then hold position at the waypoint for a user specified time. The primary purpose of this is to allow enough time for sensor data collection. To hold position at the waypoint, the addition of a PID controller on position error and the repulsive vector from (5) is used to maintain the position and avoid obstacles when holding position, i.e.,

$$\mathbf{v}_{\text{hold}} = K_{\text{p}}\mathbf{e}_{\text{pos}} + K_{\text{i}} \int \mathbf{e}_{\text{pos}} dt + K_{\text{d}}\dot{\mathbf{e}}_{\text{pos}} + \mathbf{f}. \tag{9}$$

While holding position the yaw controller rotates the robot in the direction of the next waypoint. This insures a smooth start when the wait time is over.

C. Experimental Results

Extensive testing was performed outdoors to ensure reliable collision-free flight. The magnitude of the action vector $\mathbf{v}$ is saturated to a maximum allowable speed that allows the robot to remain agile in all directions. For the Enif aerial robot, this was found experimentally to be 1 m/s. The value of parameter c in (8) was found to work best at 0.55 in the outdoor environments tested.

The experiment shown in Fig. 10 was carried out in an outdoor environment with the target waypoint set inside a fenced area with an opening (gateway). The commanded speed was 1 m/s. The robot successfully avoided the walls, traveled through the gateway, and reached the waypoint using PF-IPA at an average speed of 0.97 m/s. The robot smoothly traveled along the walls and avoided local minimas that standard PF would have trouble navigating around. The map shown was built after the flight test to demonstrate the behavior of the aerial robot.

The root-mean-squared tracking error of raster scanning in the obstacle-free environment is experimentally determined to

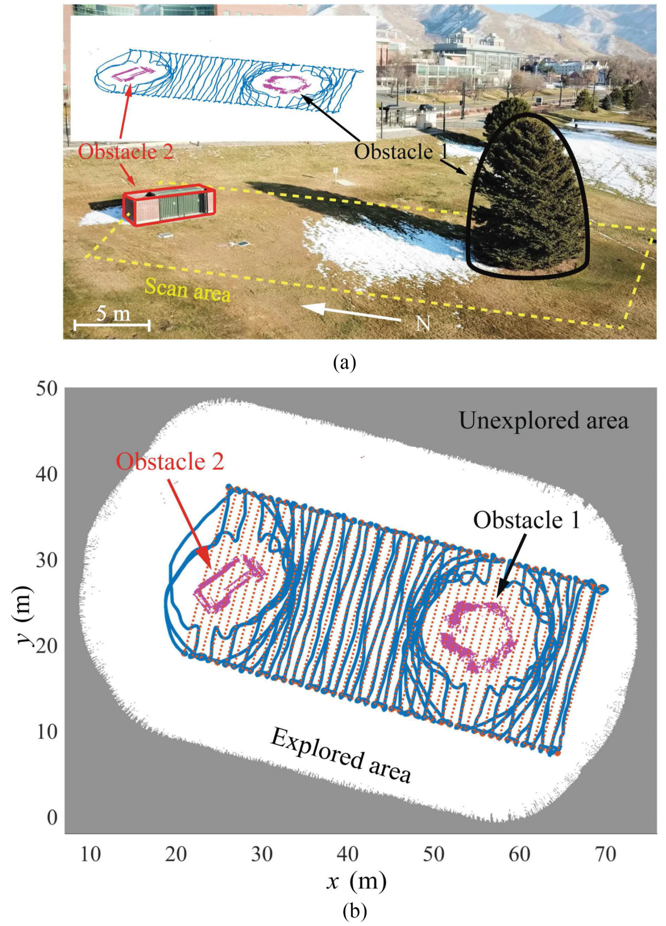

Fig. 11. Flight test of a raster scan with PF-IPA method around two obstacles. (a) Aerial photo shows the two obstacles and the scanned area. (b) Map is generated after flight for validation only. Solid blue curve shows the trajectory of the aerial robot around obstacles.

be 0.13 m. With obstacle presented, the robot outdoor collision-free guidance while performing a raster-scan pattern is shown in Fig. 11. The commanded speed was 1 m/s. The dimensions of the raster-scan pattern are 45 by 20 m with 1-m step length. The waypoint list sent to PF-IPA was the turning points at the end of each segment of the raster pattern.

As shown, the reciprocal response of $\mathbf{f}$ to the distance of obstacles causes the robot to stay a safe distance away from all obstacles. Due to the inertia added by PF-IPA, once the robot chooses a side of the obstacle to travel around, its path remains relatively smooth around the rest of the obstacle and to the waypoint.

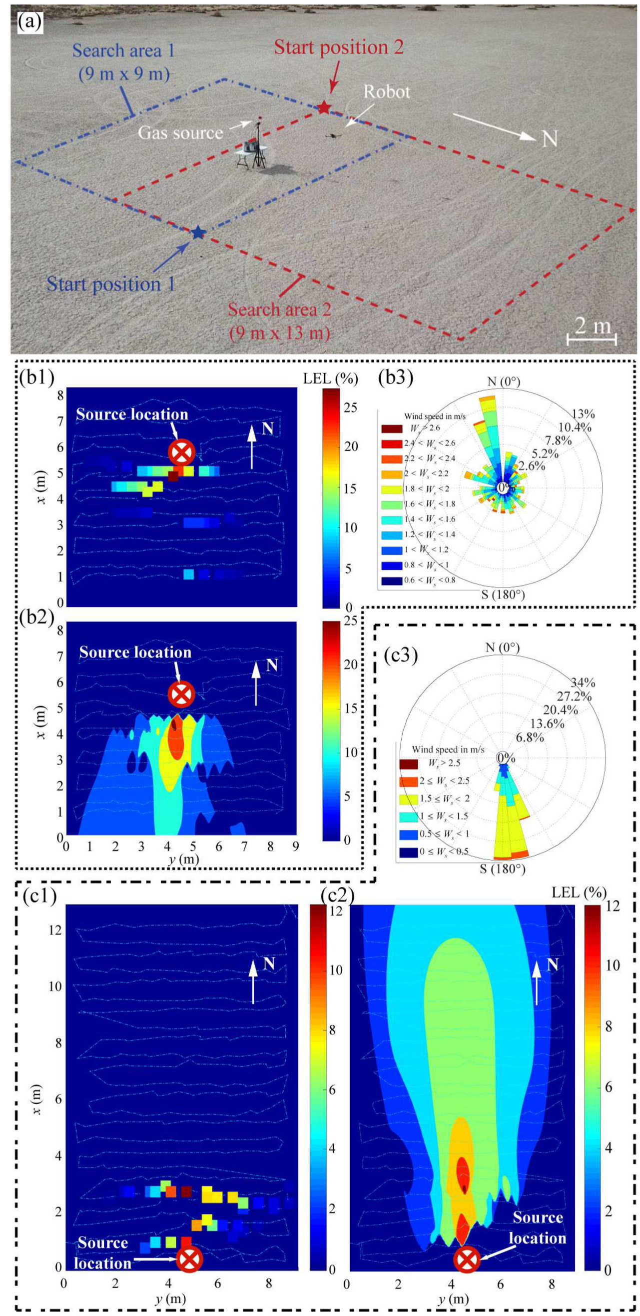

Fig. 12. Outdoor propane mapping experimental results. (a) Experimental setup showing overview of the test location, showing the relative distance between the source and the robot. The two search areas of interest and how they enclose the source. Weather conditions were sunny and calm, with an average light wind speed of approximately 1.5 m/s; (b1) and (c1) show LEL measurement plots in a map of 0.2×0.2 m grid spacing; (b2) and (c2) show the %LEL mapping results using a Gaussian plume model with kernel extrapolation technique; and (b3) and (c3) are wind roses of wind condition measured by the ground station with an anemometer.

VII. Chemical Mapping Demonstration

A. Experimental Setup

An outdoor chemical sensing experiment was carried out on the salt flats of western Utah, as shown in Fig. 12. In the experiment, six propane tanks with 0–30 psi regulators were opened while the aerial robot was grounded. From the ground station, the robot was given an AOI [as shown in Fig. 12(a)], along with various scanning parameters, waypoint wait times, and maximum velocity values as shown in Table III. Also, Table III shows environmental conditions as well as other experimental setup parameters. The wait time at waypoints were picked according to the sensor frequency and robot command speed. The waypoint radius was set to be the same as the waypoint step length to ensure smooth tracking.

TABLE III
EXPERIMENTAL SETUP FOR TWO SEARCH AREAS

Parameter	Search area 1	Search area 2
Area Fig. 12(a)	9 m × 9 m	13 m × 9 m
Waypoint step length	0.5 m	0.5 m
Waypoint radius	0.5 m	0.5 m
Scanning angle	π rad	0 rad
Wait time	2 s	2 s
Command speed	0.5 m/s	0.5 m/s
Sensor frequency	0.5 Hz	0.5 Hz
Average wind	North 1.5 m/s	South 1.1 m/s
Wind	Fig. 12(b3)	Fig. 12(c3)
Total flight time	13 min	23 min
Number of propane tanks	6	6
Robot initial position	North-east	South-west

B. Experimental Results

An experiment was designed to illustrate the feasibility of the system in chemical sensing and to investigate the challenges ahead. Therefore, obstacles were not included in the chemical mapping experiment to avoid coupling effects. The following discusses the resulting concentration maps from both search areas shown in Fig. 12(b1), (c1), (b2), and (c2), and the associated problems discovered from both the experimental setup and the system. In addition to the concentration maps, Fig. 12 shows the scanning trajectories, the actual source location, and wind rose plot during the experiment (measured from the ground station).

It can be seen that the designed aerial robot can map this relatively small propane release with light and consistent winds (2 m/s). In fact, the furthest concentration measurement was 6 m away from the source [see Fig. 12(b1)]. Also, notice that the concentration level and intensity of measurements increase when measurements closer to the source location, which is consistent with various chemical plume models [3], [24]. This result provides a realistic check of the generated concentration maps.

Because of the large discontinuities and relatively low concentrations (<10% LEL) of the concentration map [see Fig. 12(b1) and (c1)], the authors believe that the turbulent conditions caused by the rotors influenced the measurement. It is believed that the rotor disturbances would have less of an effect for large scale releases. However, when releasing a large amount of propane, it is challenging to achieve consistent release rates due to cooling of the tank and fluctuations in environmental conditions. In fact, the cooling of the tanks reduced the release rate within 15 min of the start of a release.

A Gaussian plume model with the kernel extrapolation technique was used to generate the gas distribution map shown in Fig. 12(b2) and (c2) [70], [71]. By incorporating the wind direction and speed [see Fig. 12(b3) and (c3)] into the kernel, the generated maps predict average concentration values with respect to time, even in areas where the probability of detecting gas concentration is low [see Fig. 12(b2) and (c2)].

In summary, the experimental results demonstrated feasibility of the Enif system for detecting and mapping a gas release. In particular, approximately 100 and 120 m^2 search areas were scanned to create chemical concentration maps. Such maps can provide crucial data following a natural disaster or malicious attack, for example, to identify safe zones, asses risk, and monitor areas for continued exposure while keeping humans and rescuers safe.

VIII. CONCLUSION

The design and development of an autonomous chemical-sensing aerial robot system to survey and monitor large urban and suburban environments with obstacles was presented. Compared to other chemical-sensing aerial robots, the proposed system incorporates the following advancements:

1) model-based vehicle design for flight-time enhancement;
2) user-friendly ground station and basic mission control for autonomous monitoring and data collection;
3) state-of-the-art chemical sensor with the ability to identify and quantify hazardous gases;
4) real-time data visualization;
5) collision-free navigation.

The robot can autonomously scan and map an area for leaking chemicals. The user can easily control the robot and view real-time data during flight through the user-friendly ground station. Each of the features were presented and validated through experiments and outdoor mapping of a propane gas release. The results demonstrated the overall effectiveness of the autonomous environmental monitoring system.

REFERENCES

[1] R. Marchant and F. Ramos, “Bayesian optimisation for intelligent environmental monitoring,” in *Proc. IEEE Int. Conf. Intell. Robot. Syst.*, Vilamoura, Portugal, 2012, pp. 2242–2249.
[2] A. Marjovi and L. Marques, “Swarm robotic plume tracking for intermittent and time-variant odor dispersion,” in *Proc. Eur. Conf. Mobile Robots*, Barcelona, Spain, 2013, pp. 379–384.
[3] M. Hutchinson, H. Oh, and W. Chen, “A review of source term estimation methods for atmospheric dispersion events using static or mobile sensors,” *Inf. Fusion*, vol. 36, pp. 130–148, 2017.
[4] H. Ishida, Y. Wada, and H. Matsukura, “Chemical sensing in robotic applications: A review,” *IEEE Sensors J.*, vol. 12, no. 11, pp. 3163–3173, Nov. 2012.
[5] PHMSA. (2017). [Onine]. Available: https://www.phmsa.dot.gov/data-and-statistics/pipeline/pipeline-incident-20-year-trends
[6] A. Makeenkov, I. Lapitskiy, A. Somov, and A. Baranov, “Flammable gases and vapors of flammable liquids: Monitoring with infrared sensor node,” *Sensors Actuators B: Chem.*, vol. 209, pp. 1102–1107, 2015.
[7] T. F. Villa, F. Gonzalez, B. Miljievic, Z. D. Ristovski, and L. Morawska, “An overview of small unmanned aerial vehicles for air quality measurements: Present applications and future prospectives,” *Sensors*, vol. 16, no. 7, p. 1072, 2016.
[8] P. Neumann, H. Kohlhoff, D. Hüllmann, A. J. Lilienthal, and M. Kluge, “Bringing mobile robot olfaction to the next dimension UAV-based remote sensing of gas clouds and source localization,” in *Proc. IEEE Int. Conf. Robot. Autom.*, Singapore, 2017, pp. 3910–3916.
[9] P. Neumann, S. Asadi, J. Schiller, A. J. Lilienthal, and M. Bartholmai, “An artificial potential field based sampling strategy for a gas-sensitive micro-drone,” in *Proc. IROS Workshop Robot. Environmental Monit.*, San Francisco, CA, USA, 2011, pp. 34–38.
[10] P. Neumann and M. Bartholmai, “Real-time wind estimation on a micro unmanned aerial vehicle using its inertial measurement unit,” *Sensors Actuators A: Physical*, vol. 235, pp. 300–310, 2015.
[11] P. Neumann, S. Asadi, A. J. Lilienthal, M. Bartholmai, and J. H. Schiller, “Autonomous gas-sensitive microdrone: Wind vector estimation and gas distribution mapping,” *IEEE Robot. Autom. Mag.*, vol. 19, no. 1, pp. 50–61, Mar. 2012.
[12] P. Neumann, V. H. Bennetts, and M. Bartholmai, “Adaptive gas source localization strategies and gas distribution mapping using a gas-sensitive micro-drone,” in *Proc. Sensors Measuring Syst. Symp.*, Nuremberg, Germany, 2012, pp. 800–809.
[13] B. Luo, Q. H. Meng, J. Y. Wang, B. Sun, and Y. Wang, “Three-dimensional gas distribution mapping with a micro-drone,” in *Proc. Chin. Control Conf.*, Hangzhou, China, 2015, pp. 6011–6015.
[14] M. Rossi and D. Brunelli, “Autonomous gas detection and mapping with unmanned aerial vehicles,” *IEEE Trans. Instrum. Meas.*, vol. 65, no. 4, pp. 765–775, Apr. 2016.

[15] M. Rossi and D. Brunelli, "Gas sensing on unmanned vehicles: Challenges and opportunities," in *Proc. IEEE New Gener. Circuits Syst.*, Genova, Italy, 2017, pp. 117–120.

[16] V. Arellano-Quintana, E. Portilla-Flores, E. Merchan-Cruz, and P. Nino-Suarez, "Multirotor design optimization using a genetic algorithm," in *Proc. IEEE Int. Conf. Unmanned Aircr. Syst.*, 2016, pp. 1313–1318.

[17] Ø. Magnussen, G. Hovland, and M. Ottestad, "Multicopter UAV design optimization," in *Proc. IEEE/ASME 10th Int. Conf. Mechatronic Embedded Syst. Appl.*, 2014, pp. 1–6.

[18] D. Abeywardena, P. Pounds, D. Hunt, and G. Dissanayake, "Design and development of recopter: An open source ROS-based multi-rotor platform for research," in *Proc. Australas. Conf. Robot. Autom.*, 2015, pp. 1–10.

[19] Ø. Magnussen, M. Ottestad, and G. Hovland, "Multicopter design optimization and validation," *Model., Identification Control*, vol. 36, no. 2, pp. 67–79, 2015.

[20] H. Das, V. Baskaran, and H. Arya, "Static performance analysis of electric propulsion system in quadrotors," in *Proc. IEEE Int. Conf. Control, Instrum., Commun. Comput. Technol.*, 2016, pp. 495–500.

[21] M. Gatti, F. Giulietti, and M. Turci, "Maximum endurance for battery-powered rotary-wing aircraft," *Aerosp. Sci. Technol.*, vol. 45, pp. 174–179, 2015.

[22] U. Agarwal, "Multirotor performance optimization using genetic algorithm," in *Proc. 7th IEEE Int. Symp. Embedded Comput. Syst. Des.*, Durgapur, India, 2017, pp. 1–5.

[23] Y. Koren and J. Borenstein, "Potential field methods and their inherent limitations for mobile robot navigation," in *Proc. IEEE Int. Conf. Robot. Autom.*, Sacramento, CA, USA, 1991, pp. 1398–1404.

[24] B. Ristic, A. Gunatilaka, and Y. Wang, "Rao-Blackwell dimension reduction applied to hazardous source parameter estimation," *Signal Process.*, vol. 132, pp. 177–182, 2017.

[25] T. J. Schuyler and M. I. Guzman, "Unmanned aerial systems for monitoring trace tropospheric gases," *Atmosphere*, vol. 8, no. 10, pp. 1–16, 2017.

[26] V. M. H. Bennetts, A. J. Lilienthal, A. A. Khaliq, V. P. Sese, and M. Trincavelli, "Towards real-world gas distribution mapping and leak localization using a mobile robot with 3d and remote gas sensing capabilities," in *Proc. IEEE Int. Conf. Robot. Autom.*, Karlsruhe, Germany, 2013, pp. 2335–2340.

[27] V. Šmídl and R. Hofman, "Tracking of atmospheric release of pollution using unmanned aerial vehicles," *Atmospheric Environ.*, vol. 67, pp. 425–436, 2013.

[28] R. G. Braga, R. C. Da Silva, A. C. Ramos, and F. Mora-Camino, "UAV swarm control strategies: A case study for leak detection," in *Proc. IEEE Int. Conf. Adv. Robot.*, Hong Kong, 2017, pp. 173–178.

[29] G. Vásárhelyi *et al.*, "Outdoor flocking and formation flight with autonomous aerial robots," in *Proc. IEEE Int. Conf. Intell. Robots Syst.*, Chicago, IL, USA, 2014, pp. 3866–3873.

[30] G. M. Hoffmann, H. Huang, S. L. Waslander, and C. J. Tomlin, "Precision flight control for a multi-vehicle quadrotor helicopter testbed," *Control Eng. Pract.*, vol. 19, no. 9, pp. 1023–1036, 2011.

[31] M. Rossi, D. Brunelli, A. Adami, L. Lorenzelli, F. Menna, and F. Remondino, "Gas-drone: Portable gas sensing system on UAVs for gas leakage localization," in *Proc. IEEE Sensors*, Valencia, Spain, 2014, pp. 1431–1434.

[32] T. Kersnovski, F. Gonzalez, and K. Morton, "A UAV system for autonomous target detection and gas sensing," in *Proc. IEEE Aerosp. Conf.*, Big Sky, MT, USA, 2017, pp. 1–12.

[33] V. Gallego, M. Rossi, and D. Brunelli, "Unmanned aerial gas leakage localization and mapping using microdrones," in *Proc. IEEE Sensors Appl. Symp.*, Zadar, Croatia, 2015, pp. 1–6.

[34] Y. Mulgaonkar, M. Whitzer, B. Morgan, C. Kroninger, A. M. Harrington, and K. Vijay, "Power and weight considerations in small, agile quadrotors," in *Proc. SPIE*, vol. 9083, Baltimore, MD, USA, 2014, p. 90831Q.

[35] A. J. Rojas, L. F. Gonzalez, N. Motta, and T. F. Villa, "Design and flight testing of an integrated solar powered UAV and WSN for remote gas sensing," in *Proc. IEEE Aerosp. Conf.*, Big Sky, MT, USA, 2015, pp. 1–10.

[36] A. Lomax, W. Corso, and J. Etro, "Employing unmanned aerial vehicles (UAVs) as an element of the integrated ocean observing system," in *Proc. MTS/IEEE Proc. OCEANS*, Washington, USA, 2005, pp. 184–190.

[37] T. Donateo, L. Spedicato, and D. P. Placentino, "Design and performance evaluation of a hybrid electric power system for multicopters," *Energy Procedia*, vol. 126, pp. 1035–1042, 2017.

[38] B. Y. Suprapto, M. A. Heryanto, H. Suprijono, J. Muliadi, and B. Kusumoputro, "Design and development of heavy-lift hexacopter for heavy payload," in *Proc. Int. Seminar Appl. Technol. Inf. Commun.*, Oct. 2017, pp. 242–247.

[39] M. Duffy and T. Samaritano, "The lift! project–modular, electric vertical lift system," in *Proc. Amer. Helicopter Soc. Forum*, vol. 71, 2015.

[40] M. Duffy, A. E. Sevier, R. Hupp, E. Perdomo, and S. Wakayama, "Propulsion scaling methods in the era of electric flight," in *Proc. AIAA/IEEE Electric Aircr. Technol. Symp.*, 2018, pp. 1–23.

[41] F. Mohamadi, "Vertical takeoff and landing (vtol) small unmanned aerial system for monitoring oil and gas pipelines," U.S. Patent 20 140 236 390A1, Nov. 4, 2014.

[42] B. Wang, Z. Hou, Z. Liu, Q. Chen, and X. Zhu, "Preliminary design of a small unmanned battery powered tailsitter," *Int. J. Aerosp. Eng.*, vol. 2016, 2016, Art. no. 3570581.

[43] G. Avanzini, E. L. de Angelis, and F. Giulietti, "Optimal performance and sizing of a battery-powered aircraft," *Aerosp. Sci. Technol.*, vol. 59, pp. 132–144, 2016.

[44] G. Avanzini, E. L. de Angelis, F. Giulietti, and E. Minisci, "Optimal sizing of electric multirotor configurations," in *Proc. 8th EASN-CEAS Int. Workshop Manuf. Growth Innov.*, 2018, p. 00028.

[45] M. Oczipka *et al.*, "Small drones for geo-archaeology in the steppe: Locating and documenting the archaeological heritage of the Orkhon valley in Mongolia," in *Remote Sensing for Environmental Monitoring, GIS Applications, and Geology IX*, vol. 7478. International Society for Optics and Photonics, Berlin, Germany, 2009.

[46] C. Eschmann, C.-M. Kuo, C.-H. Kuo, and C. Boller, "Unmanned aircraft systems for remote building inspection and monitoring," in *Proc. 6th Eur. Workshop Structural Health Monit.*, vol. 36, Dresden, Germany, 2012, pp.1179–1186.

[47] S. Huh, D. H. Shim, and J. Kim, "Integrated navigation system using camera and gimbaled laser scanner for indoor and outdoor autonomous flight of uavs," in *Proc. IEEE/RSJ Int. Conf. Intell. Robots Syst.*, 2013, pp. 3158–3163.

[48] A. Abdilla, A. Richards, and S. Burrow, "Power and endurance modelling of battery-powered rotorcraft," in *Proc. IEEE/RSJ Int. Conf. Intell. Robots Syst.*, Hamburg, Germany, 2015, pp. 675–680.

[49] G. Hoffmann, H. Huang, S. Waslander, and C. Tomlin, "Quadrotor helicopter flight dynamics and control: Theory and experiment," in *Proc. AIAA Guid., Navigation Control Conf. Exhib.*, 2007, p. 6461.

[50] P. E. Hart, N. J. Nilsson, and B. Raphael, "A formal basis for the heuristic determination of minimum cost paths," *Syst. Sci. Cybern.*, vol. 4, no. 2, pp. 100–107, 1968.

[51] J. Q. Cui, S. Lai, X. Dong, and B. M. Chen, "Autonomous navigation of UAV in foliage," *J. Intell. Robot. Syst.: Theory Appl.*, vol. 84, no. 1–4, pp. 259–276, 2016.

[52] S. M. LaValle, "Rapidly-exploring random trees: A new tool for path planning," Iowa State University, Ames, IA, USA, Tech. Rep. 98– 11, 1998.

[53] L. E. Kavraki, P. Svestka, J.-C. Latombe, and M. H. Overmars, "Probabilistic roadmaps for path planning in high-dimensional configuration spaces," *IEEE Trans. Robot. Autom.*, vol. 12, no. 4, pp. 566–580, Aug. 1996.

[54] J. Borenstein and Y. Koren, "The vector field histogram-fast obstacle avoidance for mobile robots," *IEEE Trans. Robot. Autom.*, vol. 7, no. 3, pp. 278–288, Jun. 1991.

[55] J. Wu *et al.*, "Distributed trajectory optimization for multiple solar-powered UAVs target tracking in urban environment by adaptive grasshopper optimization algorithm," *Aerosp. Sci. Technol.*, vol. 70, pp. 497–510, 2017.

[56] D. Shim, H. Chung, H. J. Kim, and S. Sastry, "Autonomous exploration in unknown urban environments for unmanned aerial vehicles," in *Proc. AIAA Guid., Navigation, Control Conf. Exhib.*, San Francisco, CA, USA, 2005, p. 6478.

[57] K. Mohta *et al.*, "Experiments in fast, autonomous, GPS-denied quadrotor flight," in *Proc. IEEE Int. Conf. Robot. Autom.*, Brisbane, Australia, 2018, pp. 7832–7839.

[58] J. Minguez and L. Montano, "Nearness diagram (ND) navigation: Collision avoidance in troublesome scenarios," *IEEE Trans. Robot. Autom.*, vol. 20, no. 1, pp. 45–59, Feb. 2004.

[59] O. Khatib, "Real-time obstacle avoidance for manipulators and mobile robots," *Int. J. Robot. Res.*, vol. 5, no. 1, pp. 90–98, 1986.

[60] R. C. Arkin, "Motor schema-based mobile robot navigation," *Int. J. Robot. Res.*, vol. 8, no. 4, pp. 92–112, 1989.

[61] T. Balch and R. Arkin, "Avoiding the past: A simple but effective strategy for reactive navigation," in *Proc. IEEE Int. Conf. Robot. Autom.*, 1993, pp. 678–685.

[62] T-Motor 4004. (2017). [Online]. Available: http://store-en.tmotor.com/goods.php?id=438

[63] Hobbyking Lipo finder. (2017). [Online]. Available: https://hobbyking.com/en_us/lipo.html

[64] B. Rogers, S. Malekos, L. Deal, R. Whitten, and J. Adams, "Combined, solid-state molecular property and gamma spectrometers for CBRN&E detection," in *Proc. IEEE Int. Conf. Technol. Homeland Secur.*, 2013, pp. 607–612.
[65] A. J. Lilienthal, A. Loutfi, and T. Duckett, "Airborne chemical sensing with mobile robots," *Sensors*, vol. 6, no. 11, pp. 1616–1678, 2006.
[66] D. James, S. M. Scott, Z. Ali, and W. T. O'Hare, "Chemical sensors for electronic nose systems," *Microchimica Acta*, vol. 149, no. 1–2, pp. 1–17, 2005.
[67] V. Bennetts, E. Schaffernicht, V. Pomareda, A. J. Lilienthal, S. Marco, and M. Trincavelli, "Combining non selective gas sensors on a mobile robot for identification and mapping of multiple chemical compounds," *Sensors*, vol. 14, no. 9, pp. 17 331–17 352, 2014.
[68] K. Arshak, E. Moore, G. M. Lyons, J. Harris, and S. Clifford, "A review of gas sensors employed in electronic nose applications," *Sensor Rev.*, vol. 24, no. 2, pp. 181–198, 2004.
[69] M. Quigley *et al.*, "ROS: An open-source robot operating system," in *Proc. ICRA Workshop Open Source Softw.*, 2009, p. 5.
[70] A. J. Lilienthal, M. Reggente, M. Trincavelli, J. L. Blanco, and J. Gonzalez, "A statistical approach to gas distribution modelling with mobile robots-the Kernel DM+V algorithm," in *Proc. IEEE/RSJ Int. Conf. Intell. Robots Syst.*, 2009, pp. 570–576.
[71] E. Holzbecher, *Environmental Modelling Using Matlab*. Springer-Verlag, Heidelberg, Germany, 2012.

Xiang He received the B.S. and M.S. degrees in automation science and electrical engineering from Beihang University, Beijing, China, in 2012 and 2015, respectively. He is currently working toward the Ph.D. degree at the Design, Automation, Robotics, and Control (DARC) Lab at the University of Utah in Salt Lake City, UT, USA.

His research interests include aerial robotics, control theory, motion planning, environmental monitoring, and rotorcraft aerodynamics.

Joseph R. Bourne received the B.S. degree in mechanical engineering from the University of Utah, Salt Lake City, UT, USA, in 2015. He is currently working toward the Ph.D. degree at the Design, Automation, Robotics, and Control (DARC) Lab at the University of Utah.

His research interests include motion planning, control, Bayesian estimation, and infotaxis with application to aerial vehicles for chemical sensing and environmental monitoring.

Jake A. Steiner received the B.S. degree in mechanical engineering from the California State University Maritime Academy, Vallejo, CA, USA, in 2016. He is currently working toward the Ph.D. degree at the Design, Automation, Robotics, and Control (DARC) Lab at the University of Utah in Salt Lake City, UT, USA.

His research interests include motion planning, control, collision avoidance, and soft polymer actuators.

Cole Mortensen is working toward the undergraduate degree in computer engineering at the University of Utah in Salt Lake City, UT, USA.

His research interests include embedded systems, robotic hardware and software integration, and software design.

Kyle C. Hoffman received the B.S. degree in mechanical engineering from Brigham Young University-Idaho, Rexburg, ID, USA, in 2009. He received the M.S. degree in mechanical engineering, while performing research at the Design, Automation, Robotics, and Control (DARC) Lab at the University of Utah in Salt Lake City, UT, USA.

From 2010 to the present, he has supported engineering efforts for the U.S. Air Force as a civilian. His research interests include chemical sensors, unmanned aerial vehicle-based applications, and particle swarm optimization.

Mr. Hoffman was the recipient of a Fellowship through the U.S Department of Defense Science, Mathematics And Research for Transformation (SMART) Scholarship for Service Program in 2016.

Christopher J. Dudley received the B.S. and the M.S. degrees in mechanical engineering from the University of Nevada, Reno, NV, USA, in 2011 and 2014, respectively.

He joined Nevada Nanotech Systems, Sparks, NV, USA, in August 2014, and is a Senior Sensor Engineer focusing on design and performance of MEMS gas sensor systems.

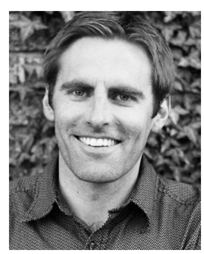

Ben Rogers received the B.S. and M.S. degrees in mechanical engineering from the University of Nevada, Reno, NV, USA, in 2001 and 2002, respectively.

He has worked with Nanogen, Oak Ridge National Laboratory, Oak Ridge, TN, USA, and he is currently a Principal Engineer with Nevada Nanotech Systems, Sparks, NV, USA. His research interests include nanotechnology, especially scanning probe microscopy and biosensors.

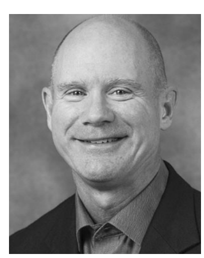

Donald M. Cropek received the Ph.D. degree in analytical chemistry from the University of Illinois Urbana-Champaign, IL, USA, in 1991.

He is the Director of the Environmental Chemistry Laboratory and the Synthetic Biology Laboratory at the U.S. Army Corps of Engineers, ERDC-CERL, in Champaign, IL, USA. His research interests include miniaturized sensing modalities for environmental assessment, biosensing and biomimetics, and smart multifunctional polymer films and coatings.

Kam K. Leang (M'02) received the B.S. and M.S. degrees in mechanical engineering from the University of Utah, Salt Lake City, UT, USA, in 1997 and 1999, respectively, and the Ph.D. degree from the University of Washington, Seattle, WA, USA, in December 2004.

He is an Associate Professor with the Mechanical Engineering Department at the University of Utah, where he joined in July 2014 and directs the Design, Automation, Robotics and Control (DARC) Lab. He is also a core member of the University of Utah Robotics Center. Between 2008 and 2014, he was at the University of Nevada, Reno, NV, USA. His research interests include modeling and control for high-speed nanopositioning and scanning probe microscopy; modeling, control, and manufacturing of electroactive polymers for applications in soft robotics; and design, control, and motion planning of mobile robotic systems for applications in emergency response and environmental monitoring.

Dr. Leang is a member of ASME.